

Report for AOARD Grant FA2386-11-1-4105

**Uncovering the Physical Basis Connecting Environment and
Tribological Performance of Ultrananocrystalline Diamond**

**Submitted to:
THE ASIAN OFFICE
OF AEROSPACE RESEARCH & DEVELOPMENT**

Submitted by:

**Department of Mechanical Engineering,
National Chung Cheng University**

**Yeau-Ren Jeng, Professor
Department of Mechanical Engineering,
National Chung Cheng University,
Ming-Hsiung, Chia-Yi 621,
TAIWAN**

E-mail: imeyrj@ccu.edu.tw

Tel: 886-5-2428189

Fax: 886-5-2720589

Report Documentation Page

Form Approved
OMB No. 0704-0188

Public reporting burden for the collection of information is estimated to average 1 hour per response, including the time for reviewing instructions, searching existing data sources, gathering and maintaining the data needed, and completing and reviewing the collection of information. Send comments regarding this burden estimate or any other aspect of this collection of information, including suggestions for reducing this burden, to Washington Headquarters Services, Directorate for Information Operations and Reports, 1215 Jefferson Davis Highway, Suite 1204, Arlington VA 22202-4302. Respondents should be aware that notwithstanding any other provision of law, no person shall be subject to a penalty for failing to comply with a collection of information if it does not display a currently valid OMB control number.

| | | | |
|--|------------------------------------|---|---|
| 1. REPORT DATE 05 OCT 2012 | 2. REPORT TYPE Annual | 3. DATES COVERED 18-08-2011 to 17-08-2012 | |
| 4. TITLE AND SUBTITLE Uncovering the Physical Basis Connecting Environment and Tribological Performance of Ultrananocrystalline Diamond | | 5a. CONTRACT NUMBER | |
| | | 5b. GRANT NUMBER | |
| | | 5c. PROGRAM ELEMENT NUMBER | |
| 6. AUTHOR(S) Yeau-Ren Jeng | | 5d. PROJECT NUMBER | |
| | | 5e. TASK NUMBER | |
| | | 5f. WORK UNIT NUMBER | |
| 7. PERFORMING ORGANIZATION NAME(S) AND ADDRESS(ES) National Chung Cheng University, 168, University Road, Minh-Siung, Chia-Yi 62102, Taiwan, NA, NA | | 8. PERFORMING ORGANIZATION REPORT NUMBER N/A | |
| 9. SPONSORING/MONITORING AGENCY NAME(S) AND ADDRESS(ES) AOARD, UNIT 45002, APO, AP, 96338-5002 | | 10. SPONSOR/MONITOR'S ACRONYM(S) AOARD | |
| | | 11. SPONSOR/MONITOR'S REPORT NUMBER(S) AOARD-114105 | |
| 12. DISTRIBUTION/AVAILABILITY STATEMENT Approved for public release; distribution unlimited | | | |
| 13. SUPPLEMENTARY NOTES | | | |
| 14. ABSTRACT In the first year of this project, the researchers studied the nano-scale mechanical and tribological properties of ultrananocrystalline diamond (UNCD), which is a thin-film material known to have extremely high strength and excellent tribological properties, namely low friction, adhesion, and wear, at macroscopic scales. They have successfully grown UNCD films in house and characterized their composition and structure. They measured the surface chemical properties of these samples as well as commercial UNCD samples from their collaborator, Advanced Diamond Technologies, Inc. These measurements demonstrate the expected carbon-rich composition but with measureable amounts of surface-bound contaminants. They also performed TEM observations to investigate the grain structure of commercial UNCD films, verifying a nanoscale grain size. Finally, collaborators from U. Pennsylvania visited NCCU in June 2012. They worked together on an in-situ TEM nanoindentation methodology and obtained preliminary results characterizing the adhesion and wear behavior of computational nano-scale UNCD asperities, verifying extremely low wear particularly in comparison to Si. | | | |
| 15. SUBJECT TERMS Modelling & Simulation, multiscale modeling , Nanoscale mechanics, Ultrananocrystalline Daimond | | | |
| 16. SECURITY CLASSIFICATION OF: | | | 17. LIMITATION OF ABSTRACT Same as Report (SAR) |
| a. REPORT unclassified | b. ABSTRACT unclassified | c. THIS PAGE unclassified | |
| 19a. NAME OF RESPONSIBLE PERSON | | | |

Abstract

In the first year of this funded project, we have studied the nano-scale mechanical and tribological properties of ultrananocrystalline diamond (UNCD), which is a thin-film material known to have extremely high strength and excellent tribological properties, namely low friction, adhesion, and wear, at macroscopic scales. In this work so far, we have successfully grown UNCD films in house and characterized their composition and structure. We have measured the surface chemical properties of these samples as well as commercial UNCD samples from our collaborator, Advanced Diamond Technologies Inc. These measurements demonstrate the expected carbon-rich composition but with measureable amounts of surface-bound contaminants. We have also performed TEM observations to investigate the grain structure of commercial UNCD films, verifying a nanoscale grain size. Finally, the U. Pennsylvania research team visited CCU in June 2012. We worked together on our in-situ TEM nanoindentation methodology and obtained preliminary results characterizing the adhesion and wear behavior of computational nano-scale UNCD asperities, verifying extremely low wear particularly in comparison to Si.

Introduction

Nanotechnology is leading to the development of materials and devices whose structure and function are controlled down to the atomic scale. Many such applications have components that experience mechanical contact and sliding. However, the lack of understanding of tribology (adhesion, friction, and wear) at a fundamental level is preventing such systems from being viable. Tribology is critical due to the high surface-to-volume ratio intrinsic to small devices. Indeed, critical problems in the reliability of micro- and nano-electromechanical systems (MEMS/NEMS) devices due to friction- and wear-related failures is well documented [1, 2].

Ultrastrong coatings hold promise for addressing these problems. In particular, ultrananocrystalline diamond (UNCD) solid lubricant thin films exhibit remarkably low friction and wear at both macroscopic and nanoscopic scales [3-7]. However, variations in the gaseous environment limit this behavior [8, 9]. Specifically, friction and wear increase by orders of magnitude in dry or vacuum environments, but are extremely low in the presence of at least a small amount water vapor. The scientific basis of this effect is not established, and this inhibits the use of these coatings. Our previous work was the first to delineate the environmental regimes for low friction and wear of UNCD, and we identified new chemical mechanisms controlling friction and wear [8, 9]. We are now working to determine how and why the environmental limits of friction and wear depend on the environment, and whether these can be controlled by changing the film structure and composition. The first step in doing this is to characterize the nanoscale tribo-mechanical response of the

material.

To do this, we have studied the growth, surface chemistry, and nanotribology of UNCD films. We have begun to conduct contact and sliding studies using a novel in-situ nanoindenter inside of a transmission electron microscope. This technique allows contact and sliding to be directly observed, and thus mechanisms can be identified and understood. Both PI's have the same instrument, so progress is being enhanced via coordinated studies. Specifically, the U. Penn PI and a Ph.D. student visited CCU in June 2012

Next, in the second year of this project, we will then determine the environmental dependence of the nanotribological properties of UNCD. We will use a unique environmental x-ray photoelectron spectroscopy system to determine the state of adsorbed water on UNCD surfaces. We will then use state-of-the-art quantitative atomic force microscopy experiments in vacuum and over a range of humidities to understand the role that water plays in nanoscale friction.

Moreover, the PI at CCU also supervises multiscale simulations including molecular dynamics, energy minimization, and coarse-grained simulations of mechanical and tribological behavior of UNCD to help understand the tribological mechanisms. The simulation efforts complement the experiments by addressing mechanical aspects of the interactions as well as providing insights into the tribological response. A key outcome would be to enable broader use of these films for demanding tribological applications for the *Air Force* and beyond.

Experiment

I. Hot Filament Chemical Vapor Deposition System (HFCVD)

For UNCD film growth, we use a hot filament chemical vapor deposition system (HFCVD) at U. Penn (Fig. 1).



Fig 1. Left: the HFCVD system. Right: inside view of diamond film growth showing the gas entry tube above the heated filaments, with the sample below.

This commercial system from BlueWave Semiconductor has been customized for nanocrystalline diamond growth [10]. The UHV-compatible chamber operates a base pressure of $\sim 2 \times 10^{-3}$ Torr. Decomposition of precursor gas species is accomplished with two 0.020-in.-diameter tungsten filaments. The substrate to be coated, usually a silicon wafer, sits below the filament on a 25 mm diameter heating stage which can heat samples up to 750°C. The substrate will also be heated by the filaments themselves. Whenever new tungsten filaments were installed, a methane pretreatment was performed. With 9 sccm methane at 10-20 Torr, the filaments were

heated to approximately 1500°C for 10 minutes, then at 1800-1900°C for 5 minutes and finally for a brief moment at 2100°C to form a thin tungsten carbide layer, which prevents tungsten evaporation during subsequent film growth. As expected, there was no sign of W contamination on any samples as verified by X – ray photoemission spectroscopy. Filament temperatures are measured with an infrared pyrometer (550-3200°C).

The substrates were coated with diamond nanoparticles (ITC Inc.) which serve as nucleation sites for diamond growth. The sample is inserted into the chamber. Precursor gases of methane at 3.7 sccm and hydrogen at 90 sccm are introduced into the chamber at an operating pressure of approximately 30 Torr with the sample temperature set to ~700 °C.

II. X-Ray Photoelectron Spectroscopy (XPS)

XPS is used to characterize the composition and chemical bonding state of the top 2-4 nm of the surface of the sample. The XPS analyses were carried out with a customized X-ray photoelectron spectrometer (a VG Scienta R3000 customized for elevated pressure operation), which is extensively been described in reference [11]. Briefly, the spectrometer is equipped with a monochromatic Al K α source (VG Scienta MX 650). The electrons emitted from the specimen are collected with an electrostatic lens, whose axis is normal to the sample surface. After passing the hemispherical analyzer, the photoelectrons are detected by a two-dimensional MCP/CCD detector. In the present work, the X-ray source was run at 30 mA and 12 kV in high vacuum

(<10⁻⁸ Torr) conditions, and the analyzer was operated in constant-analyzer-energy mode. A differential pumping system operating on the analyzer and electron optics column allows XPS operation in gaseous environments, up to 0.4 Torr. This capability will be used in the future to investigate the environmental dependence of the surface chemistry as a function of exposure to water vapor.

III. Transmission electron microscopy (TEM) and In-Situ Nanoindentation

Two TEM systems have been used for the research at U. Penn. The first is a JEOL 2010F Field-Emission TEM/STEM. This is a state-of-the-art field emission transmission electron microscope with capabilities ranging from nanobeam and convergent beam diffraction to high resolution phase contrast, analytical and energy filtered imaging. The 2010F has been optimized for analytical microscopy with a large solid angle for high X-ray throughput, scanning, scanning-transmission, and backscattered electron detectors and a Gatan image filter for energy filtered imaging and electron energy loss spectroscopy. This combination of analytical capabilities makes the 2010F ideal for the characterization of a wide array of samples, but it is also a very capable high-resolution instrument with a point-to-point resolution of 0.23 nm.

The second TEM at U. Penn is a JEOL 2010 TEM, available for both conventional and high resolution TEM imaging. It is equipped with single tilt, double-tilt, heating and cooling sample holders for a wide range of imaging experiments. The analytical objective lens pole piece on this microscope allows

for sample tilting up to 45 degrees, while maintaining a point-to-point resolution of 0.25 nm. In addition to the conventional plate camera, this instrument is equipped with a Gatan Peltier cooled CCD imaging system for high quality digital imaging.

Nanoscale wear tests were conducted inside either the JEOL 2010F transmission electron microscope (TEM) at U. Penn, or inside a JEOL TEM at CCU, using an in situ nanoindentation apparatus (PI-95, Hysitron, Minneapolis, MN). A nominally flat (100)-oriented diamond punch was brought into contact with a series of sharp ($R < 100$ nm) asperities (single crystal silicon, initially terminated with silicon oxide, or UNCD). The Si tips were model PPP-CONTR, (Nanosensors, Neuchatel, Switzerland), and the UNCD tips were custom probes provided by ADT, Inc. The tips were formed by coating commercial Si cantilevers with a UNCD film. Since the asperities are comprised of the ends of AFM tips which are integrated with microcantilevers, the cantilever deflection allows us to sensitively measure the applied force. Once in contact with a given tip, the diamond was then slid laterally, with reciprocating strokes typically of 100 nm, with only the adhesive force acting (no additional applied load). The contact was separated at varying intervals throughout the wear test to measure the instantaneous adhesive force, determined by observing the tensile deflection of the calibrated cantilever upon separation. Tips of varying shape were tested, with total sliding distances ranging from 200 nm to a few μm for each test. All sliding was recorded with real-time video, and high resolution (lattice-resolved, when possible) TEM images of the asperities were taken upon each separation. In post-processing, the instantaneous asperity profile was traced using the

out-of-contact images. Then the profiles were integrated to three-dimensional shapes (assuming axisymmetry of each differential slice) to quantify the volume removed - and thus the number of atoms removed.

Approach

I. Nano-mechanics Computational Algorithm

In this approach, atoms are regarded as nodes, and their potentials are considered to be elements. It is assumed that atom, i , is located at position (x_i, y_i, z_i) with displacements u_i , v_i and w_i in the x -, y - and z -directions, respectively. By defining the nodal displacement vector for the i atom as $\{u\}_i$ and the corresponding external nodal force vector as $\{F\}_i = (f_i, g_i, h_i)^T$, the total potential energy for atom, i , can be expressed as:

$$E_i = \frac{1}{2} \sum_{j \neq i} \phi(r_{ij}) + F \left(\sum_{j \neq i} f(r_{ij}) \right) - \{u\}_i^T \{F\}_i \quad (1)$$

where the atomic distance r_{ij} is given by:

$$r_{ij} = \left\{ (x_i + u_i - x_j)^2 + (y_i + v_i - y_j)^2 + (z_i + w_i - z_j)^2 \right\}^{1/2} \quad (2)$$

The differential of the atomic distance with respect to $\{u\}_i$ can be expressed as:

$$dr_{ij} = \frac{1}{r_{ij}} [x_i + u_i - x_j, y_i + v_i - y_j, z_i + w_i - z_j] d\{u\}_i = [B] d\{u\}_i \quad (3)$$

The principle of minimum work enforces the minimization of the total energy of the whole system ($E_{\text{total}} = \sum_i E_i$) with respect to $\{u\}_i$ such that:

$$\frac{\partial E_{total}}{\partial \{u\}_i} = \sum_{j \neq i} \left[\frac{\partial F}{\partial \rho_i} \frac{\partial f}{\partial r_{ij}} + \frac{\partial F}{\partial \rho_j} \frac{\partial f}{\partial r_{ij}} + \frac{\partial \phi}{\partial r_{ij}} \right] - \{F\}_i = \{0\} \quad (4)$$

Equation (8) expresses the equilibrium equation at atom 'i', which represents the equilibrium of the forces acting on atoms 'i'.

The unbalance force, $\{\xi\}_i$, can then be defined as:

$$\{\xi\}_i = \sum_{j \neq i} \left[\frac{\partial F}{\partial \rho_i} \frac{\partial f}{\partial r_{ij}} + \frac{\partial F}{\partial \rho_j} \frac{\partial f}{\partial r_{ij}} + \frac{\partial \phi}{\partial r_{ij}} \right] - \{F\}_i \quad (5)$$

In order to solve this nonlinear equilibrium equation in an efficient iterative way, it is necessary to differentiate $\{\xi\}_i$ with respect to $\{u\}_i$, i.e.

$$d\{\xi\}_i = \left\{ \begin{array}{l} \frac{\partial^2 F}{\partial \rho_i^2} \left(\sum_{j \neq i} \frac{\partial F}{\partial \rho_i} \frac{[B]}{r_{ij}} \right) \left(\sum_{j \neq i} \frac{\partial F}{\partial \rho_j} \frac{[B]^T}{r_{ij}} \right) \\ + \sum_{j \neq i} \left\{ \left(\frac{\partial F}{\partial \rho_i} + \frac{\partial F}{\partial \rho_j} \right) \left[\left(\frac{\partial^2 f}{\partial r_{ij}^2} - \frac{1}{r_{ij}} \frac{\partial f}{\partial r_{ij}} \right) [B][B]^T + \frac{1}{r_{ij}} \frac{\partial f}{\partial r_{ij}} [I] \right] \right\} \\ + \sum_{j \neq i} \left[\left(\frac{\partial^2 \phi}{\partial r_{ij}^2} - \frac{1}{r_{ij}} \frac{\partial \phi}{\partial r_{ij}} \right) [B][B]^T + \frac{1}{r_{ij}} \frac{\partial \phi}{\partial r_{ij}} [I] \right] \end{array} \right\} d\{u\}_i \quad (6)$$

$$= [K_T]_i d\{u\}_i$$

Subsequently, the conventional finite element formulation assembly procedure can be employed to assemble Equation (8) in order to obtain the total system equation, i.e.

$$d\{\xi\} = [K_T] d\{u\} \quad (7)$$

Similarly, Equation (7) can be assembled to obtain the equilibrium equation of the total system, i.e.

$$\sum_i \xi_i = \{f\}_{internal} - \{F\}_{external} = \{0\} \quad (8)$$

In terms of the finite element formulation, Equation (11) represents the tangent stiffness equation, while the terms $\{f\}_{internal}$ and $\{F\}_{external}$ in Equation (12) denote the internal force vector and the external force vector,

respectively. The simulation adopts the Newton-Raphson iterative technique to solve Equation (12) via the displacement control scheme or force control scheme. The need to calculate the full matrix of second derivatives in Newton-Raphson method can restrain the size of the simulated system. Therefore, the present research has developed an algorithm such as the utilization of the block-diagonal Newton-Raphson method to release this limitation. One of the challenges of nano-scale simulation is to predict the long-time system level performances. Hence, there is an imminent need to develop a multi-scale technique to bridge the gap between nano-scale and micro-scale. In this follow-up project, the present research has also developed a coarse graining technique for the multi-scale simulation.

For the simulations of nano-scale thin film nanoindentation, the simulated system configurations include a perfect three-dimensional crystalline slab of atoms with a (001) surface, and an indenter has a triangular pyramidal form. In the simulation, it is assumed that the hardness of the indenter's diamond tip far exceeds that of the thin copper film. Hence the indenter deformation may be neglected during the indentation process. The simulation assumes boundary conditions in which the atoms located at the four sides and base of the simulated film are fully constrained. The interatomic potential of the substrate is modeled using the Sutton-Chen potential, which has the same functional form in an EAM potential as follows:

$$U = \sum_i U_i \quad (9)$$

$$U_i = \frac{1}{2} \sum_{j \neq i} \phi(r_{ij}) + F(\rho_i) = \varepsilon \left(\frac{1}{2} \sum_{j \neq i} \left(\frac{a}{r_{ij}} \right)^n - c \sqrt{\rho_i} \right) \quad (10)$$

where ρ_i is an electron density-like term for atom i , which is defined as:

$$\rho_i = \sum_{j \neq i} f(r_{ij}) = \sum_{j \neq i} \left(\frac{a}{r_{ij}} \right)^m \quad (11)$$

where r_{ij} is the distance between atoms i and j . The potential between the carbon and copper atoms is simulated using the Born-Mayer potential, which only produces an impulsive force. This potential has the following form:

$$\phi(r_{ij}) = A \exp[-2\alpha(r_{ij} - r_0)] \quad (12)$$

where r_{ij} is the distance between carbon atom i and substrate atom j . This modified-FEM approach is used to perform simulations of nanoindentation. The distribution of the resulting stress and strain is then examined to clarify the atomic plastic behavior induced during the nanoindentation cycle. We also performed experiments using depth-sensing indentation technique. The load-depth curves of the experiments have been compared with those of computer simulation by the present approach. The indentation size effect and void effect are explored and discussed.

In addition, this study also utilizes molecular simulations to investigate the physical characteristics and the mechanical properties of carbon nanotubes (CNTs). The present research employs the Tersoff–Brenner many-body potential [12-14] to describe the inter-atomic forces, elastic properties, molecular bond energies, and bond lengths of the nanotubes. It has been used successfully by several researchers to model straight carbon nanotubes and to generate accurate predictions of the thermal properties of carbon nanotubes. The Tersoff–Brenner many-body potential is taken to have the form:

$$E = \sum_i E_i = \frac{1}{2} \sum_{i \neq j} V_{ij} \quad (13)$$

$$V_{ij} = f_c(r_{ij})[V_R(r_{ij}) + b_{ij}V_A(r_{ij})] \quad (14)$$

Here, E is the total energy of the system, which is decomposed for convenience into site energy E_i and a bond V_{ij} . The indices i and j run over the atoms of the system, and r_{ij} is the distance from atom i to atom j . The cutoff function, $f_c(r_{ij})$, is simply taken as

$$f_c(r) = \begin{cases} 1, & r < R - D \\ \frac{1}{2} - \frac{1}{2} \sin\left[\frac{\pi}{2}(r - R)/D\right], & R - D < r < R + D \\ 0, & r > R + D \end{cases} \quad (15)$$

which has continuous value and derivative for all r , and goes from 1 to 0 in a small range around R . R is chosen to include only the first-neighbor shell for most structures of interest. The short range of the potential is numerically advantageous in many applications, and is important for the applicability of the simple ideas about coordination discussed here.

The potential itself contains a repulsive and an attractive part, V_R and V_A , that both have the exponential:

$$V_R(r) = A \exp^{-\lambda_1 r} \quad (16)$$

$$V_A(r) = B \exp^{-\lambda_2 r} \quad (17)$$

In the present work, b_{ij} is taken to have the following from:

$$b_{ij} = (1 + \beta^n \xi_{ij})^{-1/2n} \quad (18)$$

where

$$\xi_{ij} = \sum_{k \neq i, j} f_c(r_{ik}) g(\theta_{ijk}) \exp[\lambda_3^3 (r_{ij} - r_{ik})^3] \quad (19)$$

$$g(\theta_{ijk}) = 1 + \frac{c^2}{d^2} - \frac{c^2}{[d^2 + (h - \cos \theta_{ijk})^2]} \quad (20)$$

where b_{ij} measures the relative strength of the attraction between atoms i and j , which depends on the parameters β and n , and the function, ξ_{ij} , which measures the total effect of all nearby atoms on the interaction. The $f_c(r_{ij})$ is again used to remove the effect of the more distant atoms from the calculation and the angular positions of the atoms are modeled with the function, $g(\theta_{ijk})$, where θ_{ijk} is the angle between atoms j and k , measured from atom i , and the parameters A , B , λ_1 , λ_2 , λ_3 , c , d and h are determined through fitting to experimental data. The present research systematically establishes a detailed definition of the mechanical properties of carbon nanotubes during the elastic and plastic deformation.

II. Clustered atomistic-continuum mechanics (CACM)

A novel clustered atomistic-continuum mechanics (CACM) based on the atomic mechanics and nonlinear transient finite element theory is proposed herein to simulate the mechanical behavior of the nano/bulk-structure under external mechanical loading or with thermal condition. In order to reduce the computational time efficiently and makes the simulation of the mechanical behavior of nano- and bulk- structure possible, the CACM treats the specific clustered atoms or molecule groups as a clustered super-element in the modeling, e.g. the sugar-phosphate backbone of DNA, super lattice of metal,

and silicon. The cluster atom/molecule, namely super-atom/super-molecule should have the similar mechanical behavior with its discrete form. Moreover, the virtual super-element is adopted to describe the interaction energy/force between atoms or clustered-atom groups (e.g., hydrogen bond, covalent bond and other chemical bonds) via the atomic level potential energy and continuum mechanics. Furthermore, The Interfacial Element (TIE) has been introduced in CACM to bridge the interface of nano/bulk system, and with the capability of TIE, CACM should be able to tie nano and bulk (namely, local-global) structures seamless in one multi-scale system. Finally, atoms, super-atoms and continuum mechanics based finite elements all were connected in one micro-macro (namely, local-global) simulation model using minimum energy technology. A typical CACM modeling is treated as clustered beam element with characters of axial forces, bending moments and torsions. The stacking energy between adjacent base pairs is essentially van der Waal force interaction which is described by the L-J potential form:

$$\phi(r_{ij}) = 4\varepsilon \left[\left(\frac{\sigma}{r_{ij}} \right)^{12} - \left(\frac{\sigma}{r_{ij}} \right)^6 \right] \quad (21)$$

where ε is the depth of the potential well and σ is the (finite) distance at which the interparticle potential is zero and r is the distance between the particles. The molecular bonds between pairs are mechanically transferred into bending moments and forces which are expressed as:

$$F_j = \sum_i C_{(j,i)} \frac{\partial}{\partial x_i} E(R_0 + dx_i, \theta_0 + d\theta_i) \quad (22)$$

where i, j and $C_{(j,i)}$ represent the number of hydrogen bonds, different kinds of reaction forces/bending moments/torque and weighting coefficients. Note

that x_j is displacement along the hydrogen bond direction. θ_j is the angle change between donor and acceptor, and $\theta_j = f_j(dx)$, where f is the specific function with respect to j . From theoretical, simulation results and computational efficiency aspects, CACM method can provide a feasible simulation technique to bridge the gap of atomistic and continuum mechanics. The CACM, an energy-based numerical analysis/prediction method adopted in this project is very flexible, effective, and robust, it is able to handle multi-scale, multi-loading simulation and process modeling applications which is not possible for any other existing methods.

Results and Discussion

I. Growth

Figure 2 is a photograph of a Si wafer coated with a UNCD film grown at U. Penn. The films display a clear interference pattern on its surface due to the non-uniform thickness due to a temperature gradient present during growth. This in fact provides an advantage as it allows us to characterize different film properties as a function of temperature on one sample.

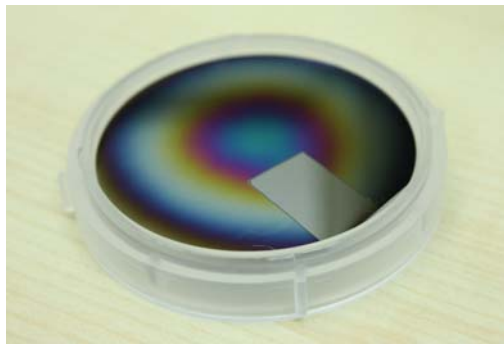


Fig. 2. NCD film partially covered during deposition

A region of the film is masked from growth, seen in the lower right sector of the wafer. Moreover, a clear contrast can be observed between the region

where NCD did not grow and the region where the film was deposited, as seen in Figure 4.

The masking was done to enable us to determine the thickness of the film. In order to avoid any optical artifact, a thin (ca. 100 nm) layer of platinum was deposited on top of the sample and a white light interferometer was used to measure the step height over the edge near the central region of the sample. This was performed for several growth times. The growth rate of the UNCD was then calculated by a least squares fit the experimental point with a line passing through the origin. The results are shown in Fig. 3. The calculated growth rate, 57 ± 5 nanometers per hour, is significantly lower than the growth rates reported in the literature which reveals growth rates of >300 nanometers per hour.

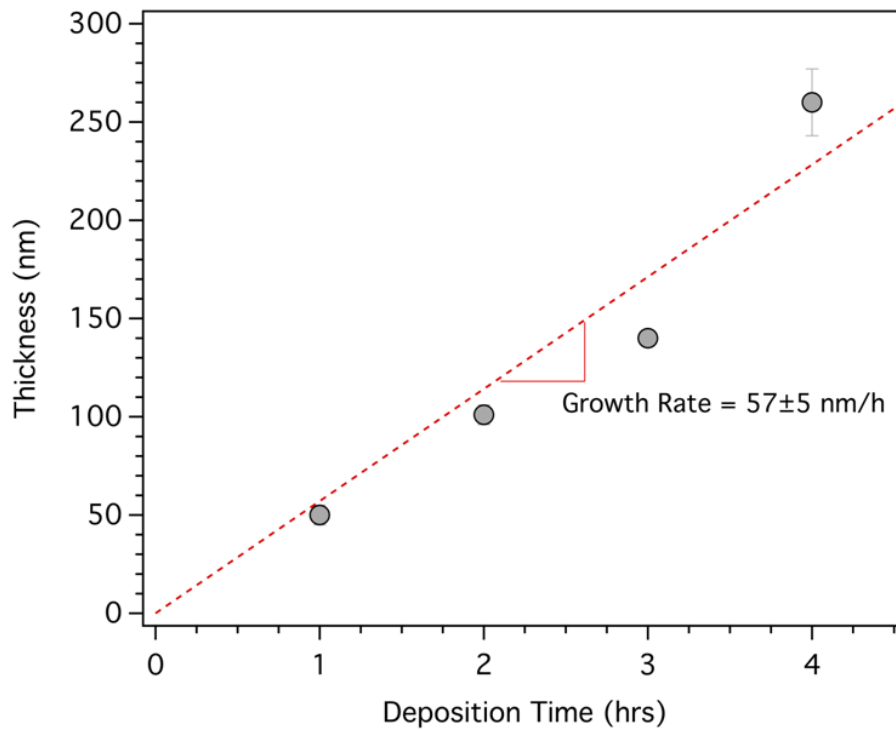


Fig. 3. Growth rate of diamond films.

Atomic force microscopy was used to characterize the film morphology.

The results are shown in Fig. 4.

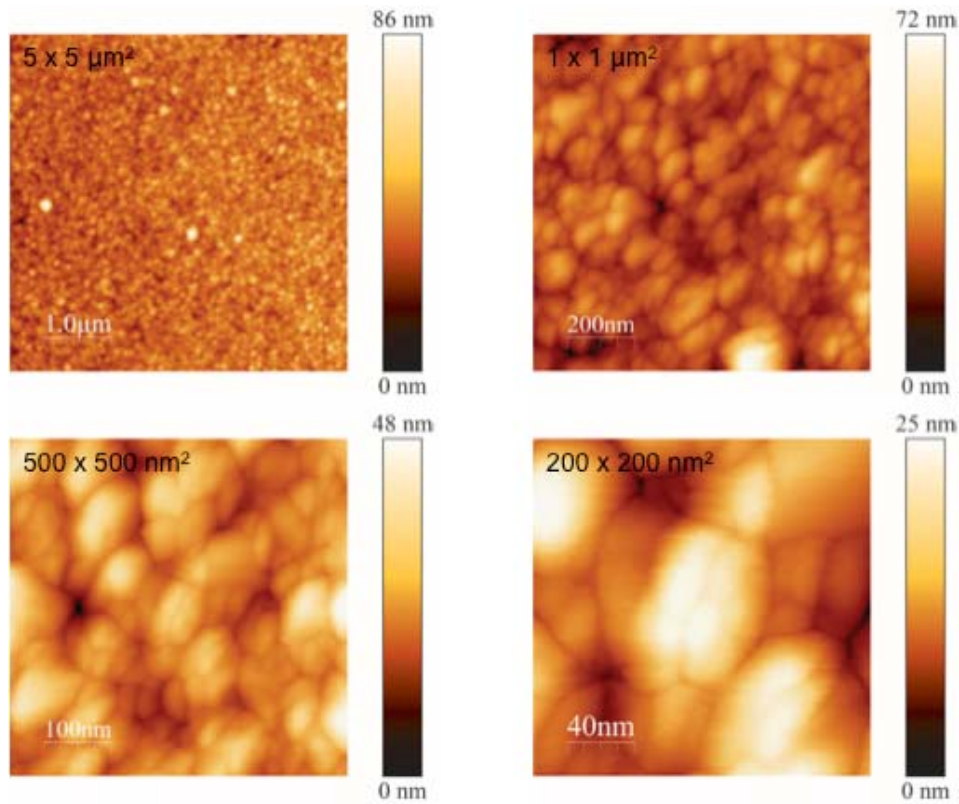


Fig. 4. AFM topographic images of the diamond films.

The AFM results reveal that the films are continuous and uniform. However, the grain size of the films, inferred by analysis of the topographic protrusions seen on the films, was in the range of 10-40 nm. This is larger than the expected grain size. The larger grain size and slower growth rate indicates that the deposition conditions are not optimal.

Additional depositions were performed with a new nanodiamond seed solution to investigate the possibility the older seed solution was contaminated, which would have caused inadequate nucleation of the surface and hindering growth. However, this did not affect the growth rate or film

morphology. We thus hypothesize that one of the flow meters is out of calibration, and thus our selected flow rates were not achieved. The results are consistent with having an excess of hydrogen in the system which slows down the growth rate. It is likely that with recalibrated flow meters, we will readily achieve a higher growth rate. We therefore plan new growth runs after the flow meters are calibrated and tested in order to produce UNCD films in-house. Commercial UNCD films were made available to us through our collaborator, ADT. Results obtained using these films will be described next.

II. XPS

An XPS survey spectrum of the UNCD sample from ADT is shown in Fig. 5. The spectrum reveals, as expected, a strong carbon peak at ~ 286 eV with the C KLL Auger peak at 1210 eV (corresponding to the X-ray energy of 1486 eV minus the Auger peak energy of ~ 273 eV). However, a significant fraction of oxygen is seen on the sample, as well as a small peak corresponding to Na. The latter is likely due to ambient contamination from exposure to open atmosphere during transportation. The oxygen is likely due to either physisorbed contamination also from exposure to open atmosphere, or chemisorbed species from dissociative adsorption of water. While it is also possible that oxygen contamination was present during the growth of this film, other compositional results from ADT are inconsistent with this hypothesis. In preliminary XPS results we have seen that exposing the UNCD to atomic hydrogen removes the contamination leaving a pure C spectrum.

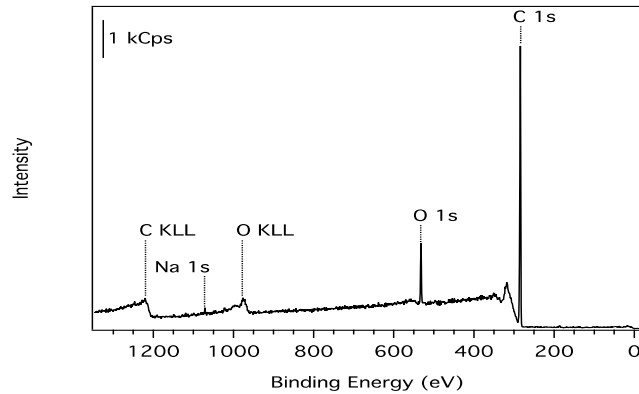


Fig. 5. XPS survey spectrum of UNCD sample from ADT, Inc.

A high-resolution spectrum of the C1s peak is shown in Fig. 6. The C1s peak is asymmetric due to the presence of covalent C-O and C=O bonds which contribute intensity at slightly higher energies than the primary C1s peak at ~285 eV. Moreover, a shoulder at lower binding energies is seen, which is due to B-C bonds as the film has a small fraction of B-doping to enhance the electrical conductivity. The broad peak at ca. 320 eV (shown in the inset of the graph) is the expected plasmon band deriving from all ($\sigma + \pi$) valence electrons.

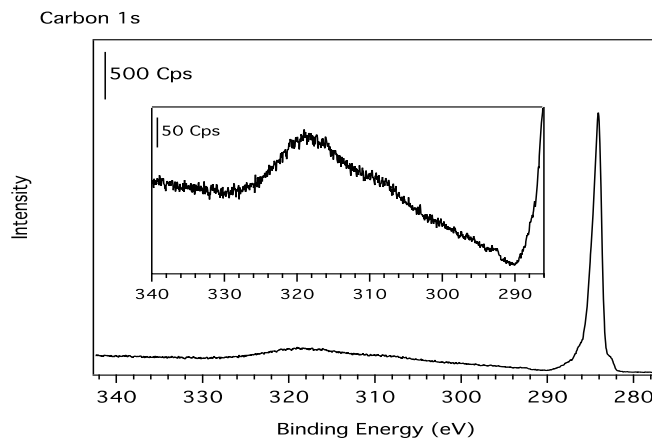


Fig. 6. High resolution C 1s XPS spectrum of the UNCD sample from ADT, Inc. The inset shows an expanded view of the high energy tail of the peak.

III. TEM

TEM images were obtained of the ADT UNCD sample. An example is shown in Fig. 7.

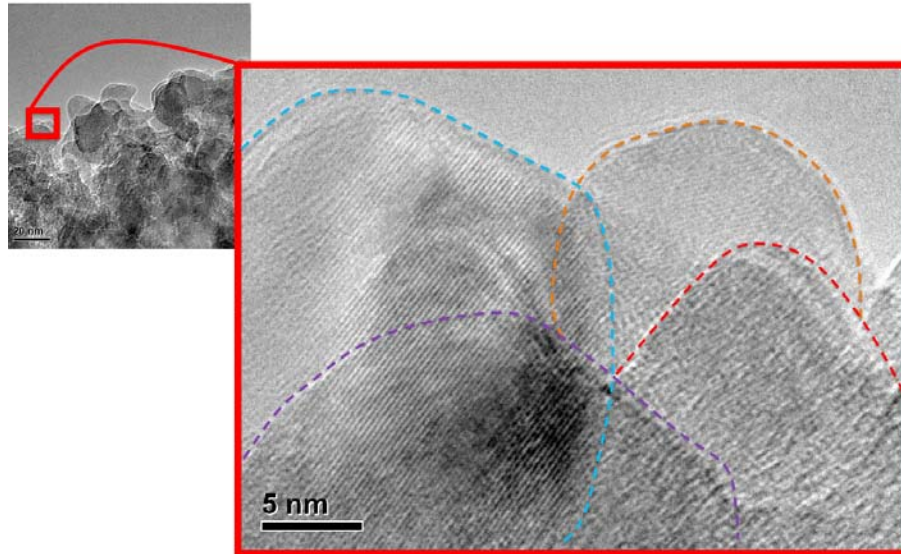


Fig. 7. High resolution TEM image of UNCD from ADT, obtained using the JEOL 2010F TEM at U. Penn. The individual diamond grains are revealed as highlighted by the dotted lines.

The image is obtained on a film that was deposited into a mold anisotropically etched into a Si wafer, and then released by etching away the Si. Thus, this portion of the film represents the very “bottom” or initial growth surface of the film. This surface is technologically relevant because that is the surface which is exposed in manufacturing of UNCD AFM probes, and thus which makes contact with samples of interest in any AFM-based application.

The TEM reveals that the UNCD is uniform with crystalline grains as seen in the expanded image on the left, where diamond lattice fringes are observed. Separate diffraction data obtained with the TEM confirm that the lattice corresponds to diamond. The individual grains are seen to vary in size from

10-20 nm. This is on the upper end of the size scale expected for UNCD films.

IV. In-situ observation of micro-structure changes of nanomaterials

An in-situ pico-indentation in a TEM has been enabled us to relate the force-displacement function to the microstructure changes of a material and made the way to track the movement of nanomaterials at small scale possible. Our study presents the utilization of such an *in-situ* characterization technique to a variety of applications.

For its application to carbon nanotube (CNT), a series of experimental nanoindentation tests has been employed to investigate buckling instabilities of CNT probes. Through the use of *in-situ* pico-indentation technique, this study relates the depth-sensing function to the microstructure changes of CNTs (see Fig. 8), in which a high-resolution TEM image is entitled to observe that the special pattern consists of multiple rippling on the compressive side of the tube walls. This phenomenon is most likely attributed to buckling instabilities of the nanotube associated with a release of the local compressive stress. The appearance of this plateau is significantly non-repetitive in the present nanotube and we interpret it as local buckling (i.e. Euler buckling) in nanotubes. A similar observation is consistent with the findings of a multi-walled carbon nanotube (MWCNTs) under compression by Yu *et al* [15].

Moreover, CNTs reinforced metal matrix nanocomposites have been fabricated by a molecular level process to investigate the nano-mechanism for enhancement of martial strength through its buckling behavior. Fig. 9 presents

SEM images showing the microstructure of a typical CNT/Cu composite sample. As shown, the sample surface contains dispersed bulge-like features. These features imply that the addition of the CNTs to the pure Cu matrix induces additional nucleation sites, which lead in turn to a greater surface roughness. The cross-sectional TEM images of the CNT/Cu composite shown in Fig. 10 show that the CNTs retain an aligned morphology following the consolidation and mechanical polishing processes. In addition, Fig. 10 and the high-resolution TEM image presented in Fig. 11 together with the selected area diffraction pattern (SADP) show that the CNTs are embedded within the interior of the Cu nanocrystals. From inspection, the grain size of the CNT/Cu composite sample is found to be approximately 45~50 nm. By contrast, that of the pure Cu sample (not shown) is around 62 nm. The smaller grain size of the CNT/Cu composite suggests that the addition of CNTs to the Cu matrix suppresses dislocation motion, and therefore inhibits grain growth. Note that a similar observation was reported by Jeong et al. [16] in their investigation into the strengthening of CNT/Co nanopowders. The SADP diffraction pattern contains a small number of continuous rings and diffraction spots. Thus, it is inferred that the Cu matrix has a polycrystalline structure.

Fig. 5 presents the experimental load-displacement curves for the pure Cu sample and the CNT/Cu composite samples with CNTs of length 2.6 and 2.1 μm , respectively. In general, the error due to the substrate effect increases with increasing indentation depth and with increasing elastic mismatch between film and various substrates [17-19]. To minimize substrate effects in the nanoindentation test, the proper indentation depth has been

limited to less than 10% of the film thickness [20, 21], and thereby reasonable mechanical properties of thin film can be extracted. Fig. 12a shows the relatively continuous slope on the loading curve. By contrast, Figs. 12b and 12c can be seen that the addition of CNTs to the Cu matrix has a direct effect on the initial slope of the load-displacement curve. Specifically, for a constant indentation force, the indentation depth reduces following CNT addition. This implies that the addition of CNTs results in a strengthening of the metal matrix [17, 18]. This observation can be attributed to the fact that the addition of CNTs may be restrained dislocation nucleation and motion, thereby leading to a rising in the mechanical strength [19]. Fig. 12b, corresponding to the composite sample containing CNTs with a length of 2.6 μm , shows that the force increases linearly as the displacement is first increased. However, at a certain displacement (i.e. 82 nm), a discontinuity occurs in the load-displacement curve, following which there is no obvious change in the force as the displacement is increased to 124 nm. The flattening of the curve indicates that a softening of the CNT/Cu composite occurs at displacements in the range of 82 to 124 nm. For the composite sample containing the shorter CNTs [Fig. 5c], the flat plateau is replaced by a sharp increase in the slope, which indicates a stiffening of the CNT/Cu composite. This stiffening effect is most likely the result of the buckling instability of the CNTs (see Fig. 13), which permits the release of the internal compressive stress as the composite is deformed [20-22]. The present findings are consistent with those of previous studies [23-25], in which it was shown that shorter single-walled CNTs deform through locally sharp kinking analogous to a local buckling. Remarkably, our experimental observations of buckling models are similar to

the recent study of the compression in aligned CNT composites [26], in which the transformation between Euler-type buckling for small nanotubes and local kinking for larger diameter nanotubes was exhibited in the CNT/polymer-composites.

Table 1 summarizes the mechanical properties of the pure Cu sample and the two CNT/Cu composite samples. Note that nine nanoindentation tests were performed on each sample. The average values of the Young's modulus and hardness for each sample are presented in Table 1. Note that the experimental errors are ± 0.35 GPa for the Young's modulus and ± 4.8 MPa for the hardness. It is evident that the addition of CNTs leads to a significant improvement in the mechanical properties of the pure Cu matrix. In addition, it is observed that the composite sample with the shorter CNTs has a greater mechanical strength than that with the longer CNTs. Interestingly, a similar phenomenon was noted by nanoindentation study into the compression of CNTs by Waters et al. [27, 28].

Table 1. Critical stress (σ_{cr}), critical buckling strain (ϵ_{cr}), Young's modulus (Y), and hardness (H) of Cu matrix and CNT/Cu composites.

| Samples | Nanotube parameters | | | σ_{cr} (μN) | ϵ_{cr} (nm) | Y (GPa) | H (MPa) |
|---------|---------------------|------------------|-----------------------------|------------------------------------|-------------------------|--------------|--------------|
| | Vol. of CNTs (%) | Diameter (nm) | Length (μm) | | | | |
| Cu | — | — | — | 47.25 | 58 | 6.75 | 80.53 |
| CNT/Cu | 5 | 21 | 2.6 | 55.67 | 82 | 8.98 | 85.21 |
| CNT/Cu | 5 | 17 | 2.1 | 92.38 | 109 | 10.17 | 96.26 |

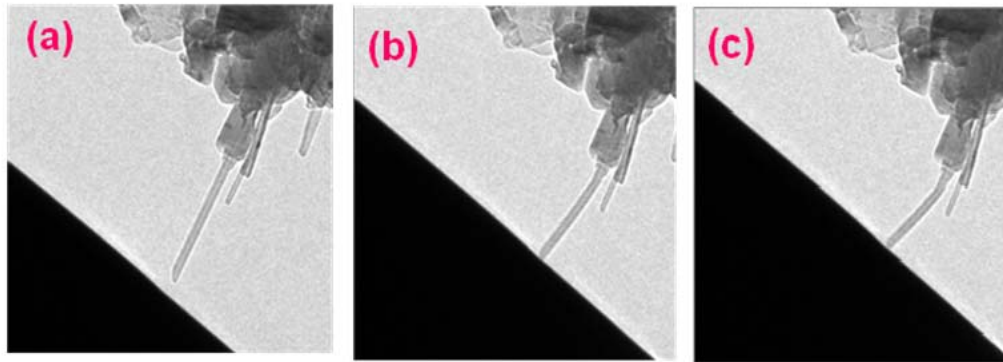
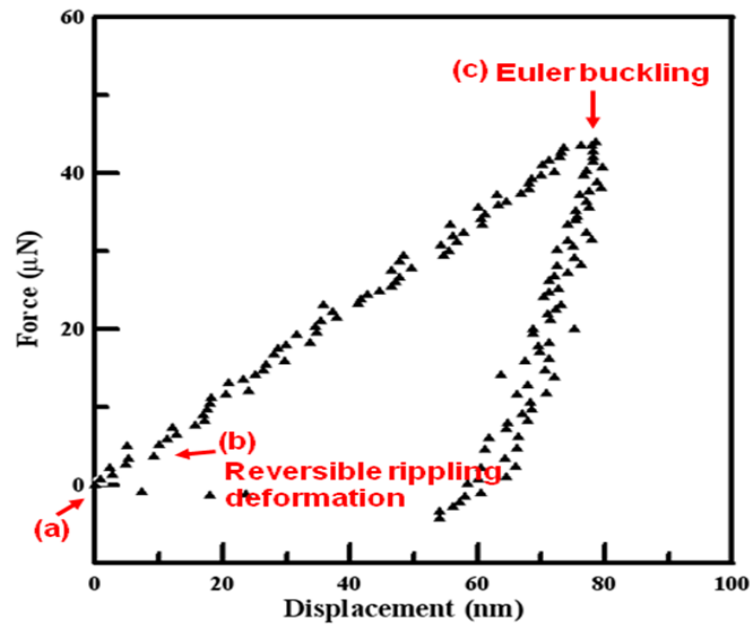


Fig.8 Representative force-displacement curves during experimental nanoindentation test. [Note that snapshots (a)-(c) denote different stages of the local-buckling processes.]

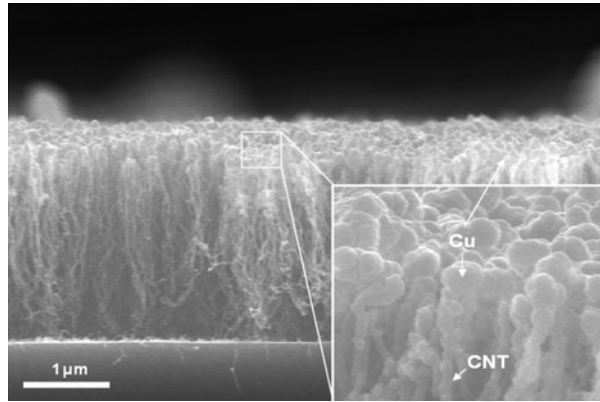


Fig.9 SEM images showing microstructure of typical CNT/Cu composite before consolidation.

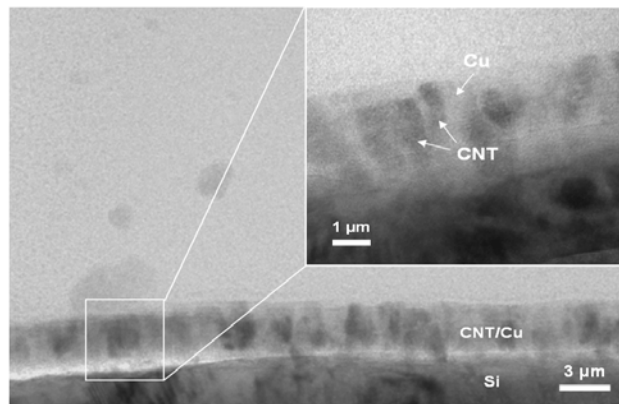


Fig.10 Cross-sectional TEM images of CNT/Cu composite following consolidation and mechanical polishing.

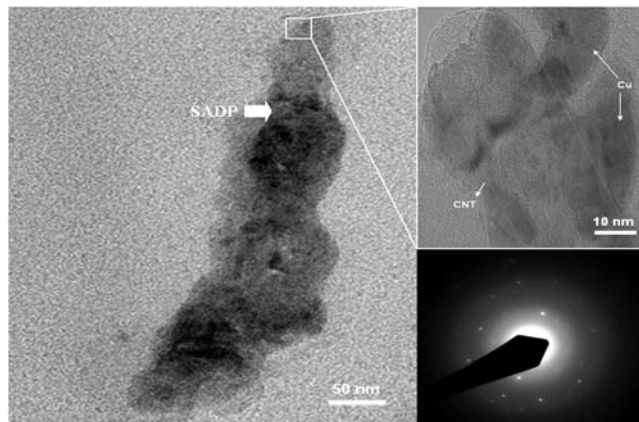


Fig.11 HRTEM images and selected area diffraction pattern of CNT/Cu composite.

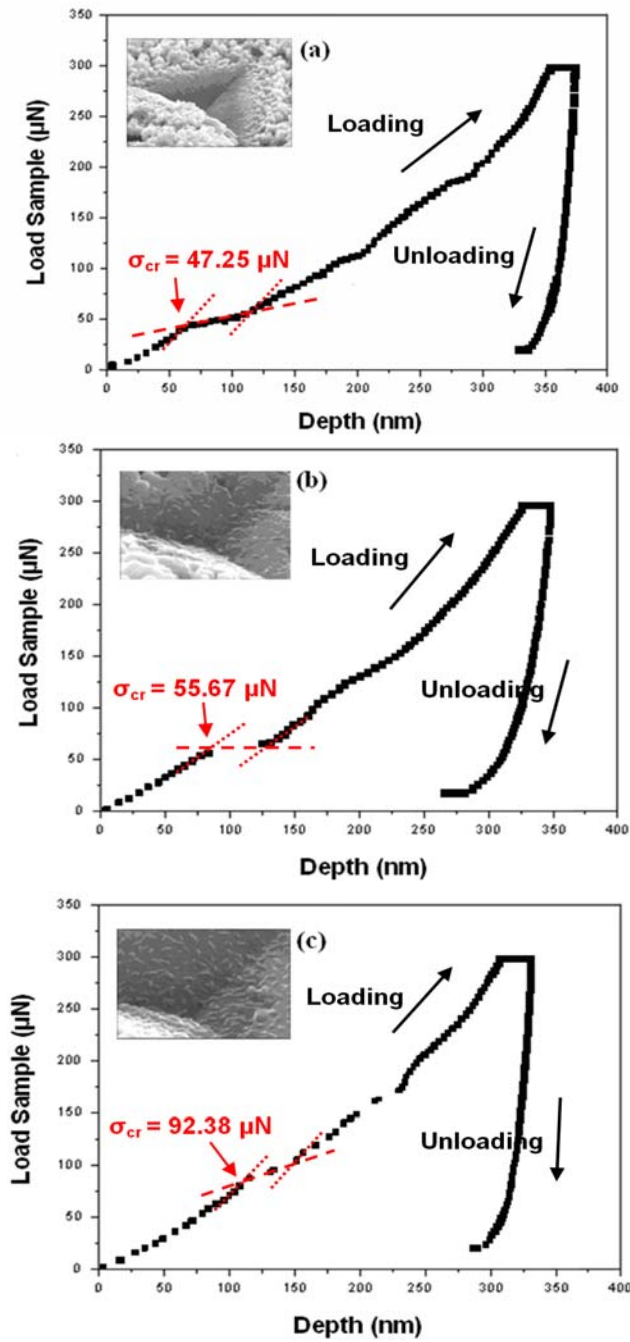


Fig.12 Representative load-displacement curves obtained from experimental nanoindentation tests: (a) Cu matrix with no CNT addition, (b) CNT/Cu composite containing CNTs of length 2.6 μm, and (c) CNT/Cu composite containing CNTs of length 2.1 μm.

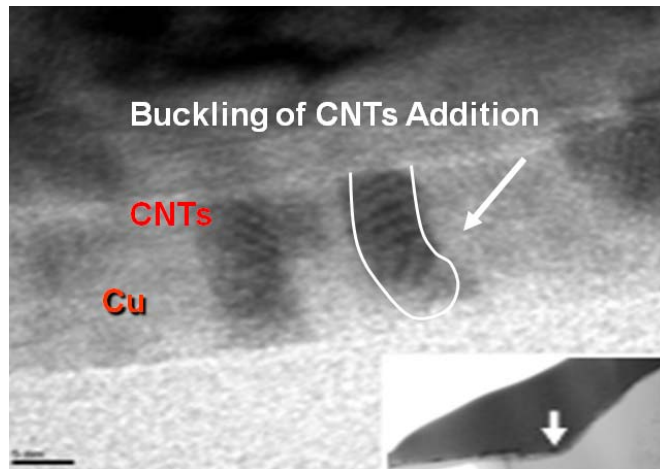


Fig.13 TEM micrographs of nanotube buckling in an aligned composite. [Note that the typical Euler-type buckling observed for longer carbon nanotubes.]

V. In-situ TEM Wear Testing

Nanoindentation tests were conducted at CCU during the visit by the U. Penn Ph.D. student. During this visit, a number of skills were transferred between the CCU and Penn teams, including methodology for use of a Hysitron triboindenter, use of the in-site TEM PicoIndenter, use of the TEM itself, MATLAB scripts for data analysis, sample preparation methods, and various simulation and experimental methodologies relevant to the research program. The CCU TEM users were trained on use of specimen tilt, and given a brief tutorial on diffraction by the U. Penn team. Noise tests of the CCU PicoIndenter were also performed. The team found that the vibration amplitude of the PicoIndenter at CCU is on a par with the baseline noise observed in Penn's system. A mechanical system resonance exists at ~123 Hz, with an EMI peak observed at 120 Hz (2x line frequency). When the

system is at rest, a standard deviation of position is observed to be 3 nm (measured at 1000 pts/s, with the instrument's "Qgain" setting set to 4). These are within the vendor's specifications for the instrument.

The team established a common procedure for TEM wear testing that involved initial imaging of probes via TEM, obtaining videos of approach/contact/retract measurements followed by imaging (usually capture 5-10 good pull-offs on video), and obtaining videos of sliding at adhesion-only loading (with higher resolution still images after each video). Images were obtained before sliding, and then after sliding distances of 200, 400, 800, 1600, 3200, and 6400 nm. Additional tests were performed by sliding under higher applied loads; analysis of this data is still in progress and so results reported here focus on the experiments performed under zero applied load.

Results for one Si probe (tested at U. Penn), and two UNCD probes (tested at CCU) are shown in Fig. 14.

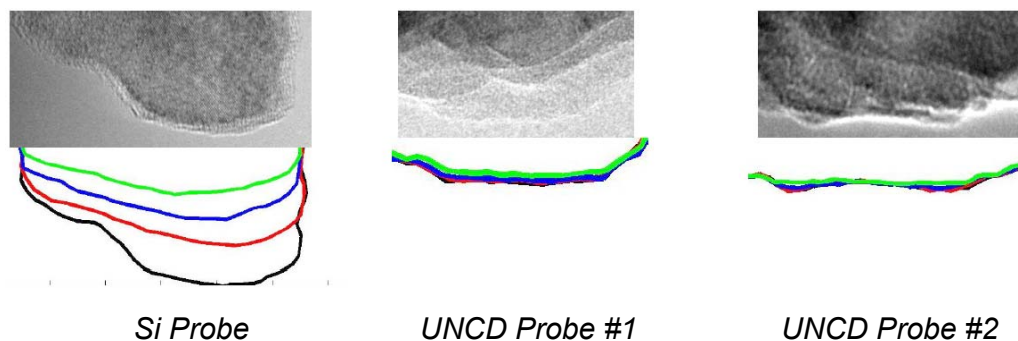


Fig. 14. Top row: High resolution TEM images of the tested probes before any wear occurred. Bottom row: overlaid traces of the outer edge of the probes after sliding intervals of 200, 400, 800, 1600, 3200, and 6400 nm. The Si probe is seen to wear away rapidly, while barely any wear of the UNCD probe is observed.

The Si probe is seen to wear rapidly with each interval, while little wear of the UNCD probes is seen; the volume change is barely within the resolution limits of the technique. All three probes had comparable initial sizes. A plot of the worn volume vs. sliding distance is shown in Fig. 15. The plot shows quantitatively that the UNCD exhibits orders of magnitude less wear than the Si under comparable conditions. This agrees with our qualitative expectation that UNCD should exhibit less wear than Si at the nano scale, but provides unique and completely new quantitative data for such a comparison.

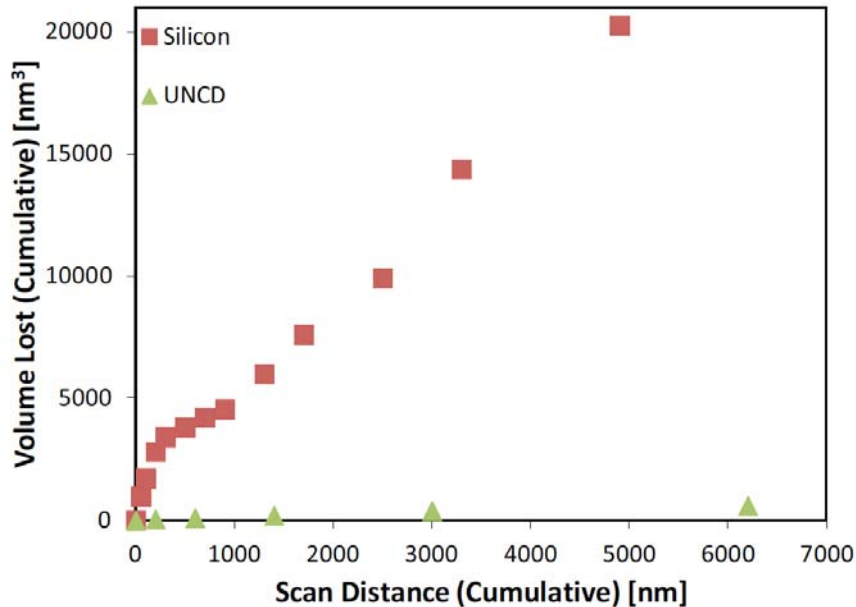


Fig. 15. Volume loss of Si nanoasperity (red squares) and for a UNCD asperity (green triangles). The UNCD exhibits orders of magnitude less wear than the Si under comparable conditions.

VI. Multiscale simulations for contact behaviors and sliding mechanisms at nano-scale interfaces

Atomistic approaches and multi-scale simulations will be focused on nanostructure mechanisms and the interfacial phenomena to identify the key physical mechanisms that control friction and wear for sliding on UNCD, and to determine how these are affected by the mechanical properties, the film structure (H-content and grain boundary structure), and the surface chemistry at nano-, meso- and macro-scales. As shown in Fig. 16, the simulation model comprises a single crystalline of diamond, hydrogen adsorbed layers and a diamond indenter. The proposed model comprises three kinds of atoms, namely boundary, thermostat, and Newtonian. A periodic boundary condition is imposed on the diamond film to prevent the overflow of the hydrogen atoms in the adsorbed layer and serve to reduce the edge effects and to maintain the lattice symmetry. Meanwhile, the atoms next the periodic boundary are treated as thermostat atoms and are modified based on the Nose–Hoover method [29] to drive the equilibrium temperature of the substrate toward the desired value.

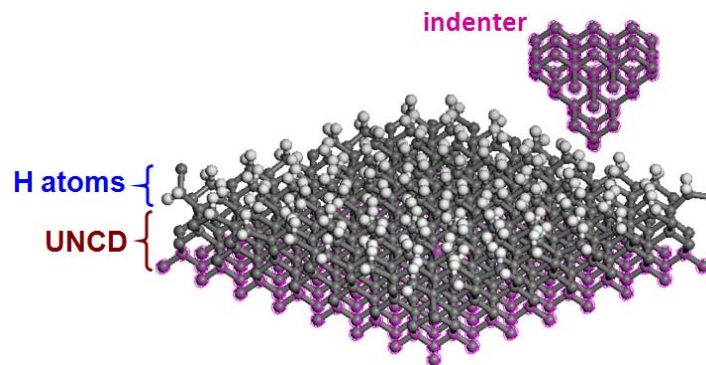


Fig. 16. Initial simulation model for nanoindentation process showing diamond crystal slab, diamond indenter and hydrogen adsorbed layer.

To further illustrate the effects of the adsorbed layer on the structural deformation of the diamond samples, Fig. 17 presents atomic configuration models which clearly show the formation of significant slip planes during the nanoscratch. Our results show the presence of slip planes aligned in the direction of the side faces of the pyramidal indenter. In general, as the indenter is pushed into the diamond sample, local polymer molecules become trapped at the indentation interface, thereby forming a cavity on the diamond surface. It is necessary to note that the diamond substrate and active polymer molecules react attractively via van der Waals interactions so that hydrogen molecules may penetrate into diamond substrate. Thus, the atomistic structure at the diamond surface can be changed depending upon the adsorption of surface species. A similar observation was also noted in the water effect on the deformation of silicon monocrystals by Tang and Zhang [30]. During the subsequent scratch stage, the hydrogen molecules remain trapped within the diamond substrate and thus the cavity grows, resulting in the formation of a rough residual depth and prompting the onset of slip planes along the edges of the indenter. However, when the substrate has no hydrogen adsorbed layer, the upper layer of the diamond substrate remains in constant contact with the indenter during nanoindentation. Following the scratch stage, the residual depth is found to have a relatively shallower penetration than that observed in the specimen with an adsorbed layer as a result of recrystallization and elastic recovery induced by the adhesion between the indenter and the diamond substrate. Note that these results are consistent with those reported by Luan and Robbins in their MD modeling of atomic contacts with and without adhesion, respectively [31]. Specifically, the

bonds between the C atoms in the diamond substrate and the C atoms in the indenter are weakened as a result of the hydrogen layers between them, and hence a poorer elastic recovery takes place. In other words, the microstructural damage caused to the diamond substrate during the nanoindentation and nanoscratch becomes more severe as the adsorbed layer thickness increases. Overall, the results imply that the presence of an adsorbed layer reduces the mechanical strength of the indented specimen, particularly for indentation depth in the nanometer regime.

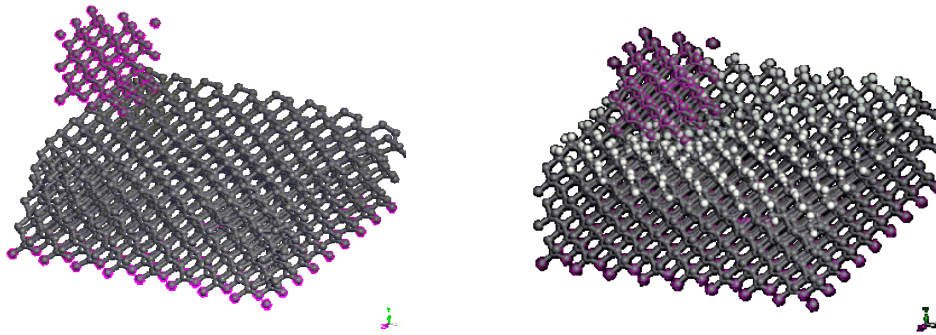


Fig. 17 Atomic configuration of diamond substrate during nanoscratch stage: (a) with and (b) without hydrogen adsorbed layers, respectively

Lateral junction growth at nano-scale is fundamental for the atomic origins of macroscopic friction and wear. Our present simulations also reveal that the lateral junction growth during incipient sliding coincides with the occurrence of dislocation in the junction. In this study, the model comprises three major components, namely a rigid carbon plate, a deformable copper asperity, and an adsorbed layer. In analyzing the junction growth mechanism, the slip vector analysis considers the $\langle 1\ 1\ 1 \rangle$ slip plane of the f.c.c. copper

lattice. In the simulations, fixed boundary conditions are imposed in the $[1\ 0\ 0]$ and $[0\ 1\ 0]$ directions, and the interactions between the carbon plate and the copper asperity are modeled using the Morse potential (See Fig. 18).

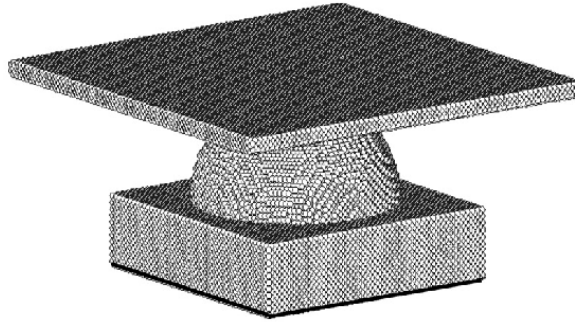


Fig. 18. Atomistic configuration of simulation system comprising single copper asperity and flat carbon plate.

Figs. 19-22 presents the variations of the normal force acting on the flat, the lateral force acting on the asperity, the tangential force coefficient, and the lateral junction growth of the asperity contact, respectively, as the lateral displacement of the rigid flat is increased. Note that in Figs. 19-21, the notation “l 1” (for example) indicates a contact interference of 1 Å. As shown in Fig. 19, the normal force decreases smoothly as the flat is first displaced in the lateral direction, but then fluctuates periodically with a sawtoothlike characteristic as the displacement is further increased. The reduction in the normal force during the initial stages of the sliding process can be attributed to slips of the asperity atoms, which lead to an increase in the contact area between the asperity and the flat [32]. Since the lateral displacement of the flat can cause the slips of asperity atoms that reduce the concentrated stress. As a result the normal force acting on the flat is decreased. A stepwise profile

of each drop of normal force can be attributed to the occurrence of slips of asperity atoms. A more detailed description of the lateral junction growth mechanism can be found in the study of Jeng and Peng [32]. Our atomistic simulation demonstrates the characteristic fluctuations of force distribution during the lateral junction process from the atomic origins.

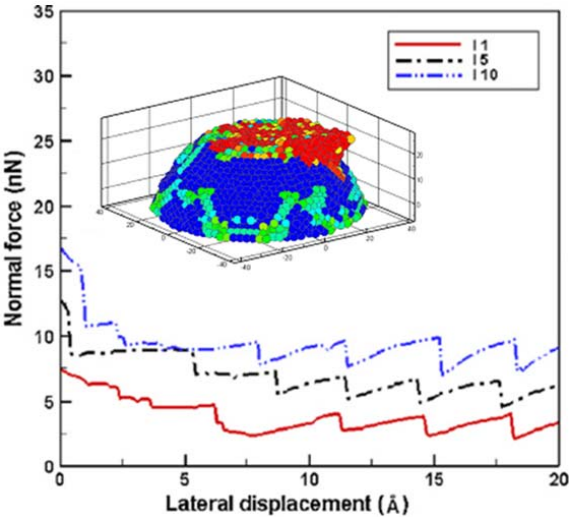


Fig. 19 Normal force acting on flat plate as function of lateral displacement

Fig. 20 shows that the lateral force increases initially with an increasing lateral displacement and then fluctuates periodically with a sawtooth-type profile; indicating the occurrence of a stick-slip phenomenon [33, 34]. From inspection, the stick-slip pattern is found to repeat at an interval of around 3 Å. According to the experimental findings presented by *Carpick et al.* [35], the period of the force fluctuation is roughly equivalent to the lattice spacing of single crystal copper. The displacement interval over which the lateral force increases continuously in Fig. 20 is roughly equivalent to that over which the normal force reduces in Fig. 19. It is reasonable, therefore, to infer that the

transition point between the smoothly increasing region of the force curve and the periodically fluctuating region coincides with the point at which lateral junction growth ceases and is replaced by stick-slip motion [33-36]. The continuum mechanics study of Brizmer et al. [37] treated the sliding inception as a plastic yield failure mechanism to determine the ends of lateral junction growth. More recently, Wu and Adams [38] suggested that the adhesion can cause the load required to initiate plastic deformation to be far less than predicted by the Hertz contact [39]. The atomistic simulation conducted in this study intrinsically accounts for the effects of adhesion and facilitates the observation of slip of atoms, which is an indication of plasticity.

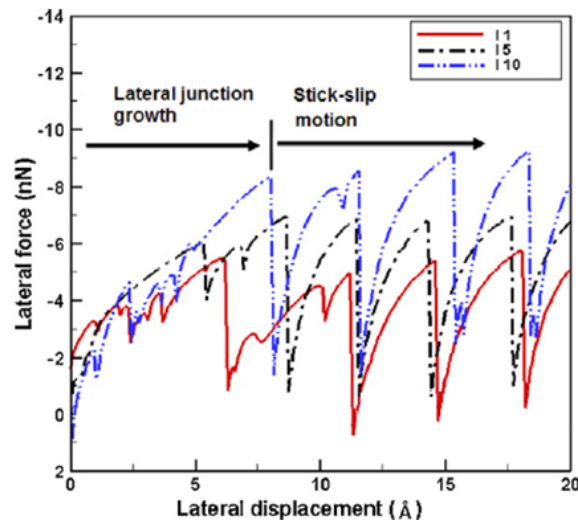


Fig. 20 Lateral force acting on asperity as function of lateral displacement

Tabor [40] introduced the tangential force coefficient, defined as the ratio of the lateral force to the normal force, to investigate the junction growth phenomenon in macroscale contacts. In this study, the same criterion is applied to investigate the lateral junction growth at the nanoscale. Fig. 21

illustrates the variation of the tangential force coefficient with the lateral displacement. The tangential force coefficient increases smoothly as the lateral displacement is increased toward 6 Å, but fluctuates periodically as the lateral displacement is further increased. The relatively high value of the tangential force coefficient is consistent with the assertion of Bowden and Young [41] that clean surfaces have a very high friction coefficient. In addition, the results presented in Fig. 21 clearly show that the tangential force coefficient is not a constant at the nanoscale, which is consistent with the finding of *Carpick et al.* [35].

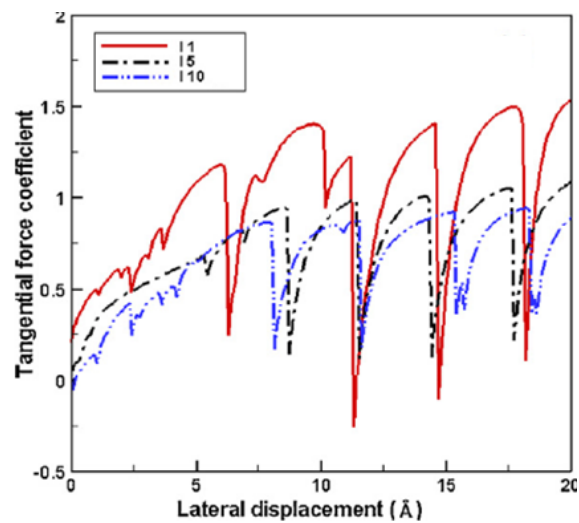


Fig. 21 Tangential force coefficient as function of lateral displacement

Fig. 22 shows the variation of the lateral junction growth as a function of the lateral displacement for various levels of contact interference for the cases without an absorbed layer. The junction growth of various lateral displacement steps is calculated by the ratio of the current contact area to that at the beginning of lateral movement. Note that in computing the size of the junction,

the boundary of the contact area is taken as the point at which the contact pressure reduces to zero [42]. The results show that for a given value of the contact interference, the lateral junction growth initially increases in a stepwise manner as the lateral displacement is increased. The lateral displacement of the flat causes the slips of asperity atoms that lead to the increase of the contact area. Hence, the lateral junction increases in a stepwise manner as the profile of the normal force is a result from the slips of the asperity atoms. However, following the onset of stick-slip motion, no further increase in the lateral junction growth occurs. The sub-figures shown in Fig. 22 demonstrate the corresponding slip vector plot for the case with contact interference 5 Å and 10 Å. The sub-figures reveal that the larger lateral junction growth for the case with a larger interference is mainly caused by the further slips of asperity atoms than that with a smaller contact interference. Overall, the simulation results provide useful insights into the atomic origins of the correlation between the evolution of the contact area and the tangential force coefficient in nanoscale contacts.

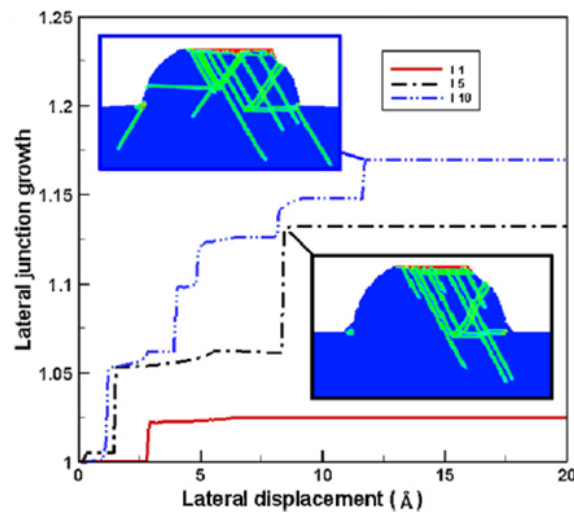


Fig. 22 Lateral junction growth as function of lateral displacement

References

1. Szlufarska, M. Chandross, R.W. Carpick, J. Phys. D: Appl. Phys. **41** (2008)123001.
2. A. D. Romig, M. T. Dugger, P. J. McWhorter, Acta Mat. **51** (2003) 5837.
3. O. Auciello, S. Pacheco, A. V. Sumant, C. Gudeman, S. Sampath, A. Datta, R. W. Carpick, V. P. Adiga, P. Zurcher, Z. Ma, H. C. Yuan, B. K. John, A. Carlisle, J. Hiller, S. Srinivasan, Microwave Magazine (2007) 61.
4. A. V. Sumant, D. S. Grierson, J. E. Gerbi, J. Birrell, U. D. Lanke, O. Auciello, J. A. Carlisle, R. W. Carpick, Adv. Mater. **17** (2005) 1039.
5. O. Auciello, J. Birrell, J. A. Carlisle, J. E. Gerbi, X. Xiao, B. Peng, H. D. Espinosa, J. Phys. Cond. Mat. **16** (2004) 539.
6. H. D. Espinosa, B. C. Prorok, B. Peng, K. H. Kim, N. Moldovan, O. Auciello, J. A. Carlisle, D. M. Gruen, D. C. Mancini, Experimental Mechanics **43** (2003) 256.
7. O. Auciello, D. M. Gruen, A. R. Krauss, A. Jayatissa, A. Sumant, J. Tucek, D. C. Mancini, N. Moldovan, A. Erdemir, D. Ersoy, M. N. Gardos, H. G. Busman, E. M. Meyer, Proc. SPIE - Int. Soc. Opt. Eng. **4235** (2001) 10.
8. A. R. Konicek, D. S. Grierson, A. V. Sumant, T. A. Friedmann, J. P. Sullivan, P. U. P. A. Gilbert, W. G. Sawyer, R. W. Carpick, Phys. Rev. B, accepted (2012).
9. A. R. Konicek, D. S. Grierson, P. U. P. A. Gilbert, W. G. Sawyer, A. V. Sumant, R. W. Carpick, Phys. Rev. Lett. **100** (2008) 235502.
10. P. J. Heaney, A. V. Sumant, C. D. Torres, R. W. Carpick, F. E. Pfefferkorn, Diam. Rel. Mat. **17** (2008) 223.
11. F. Mangolini, J. Åhlund, G.E. Wabiszewski, V. P. Adiga, P. Egberts, F. Steller, K. Backlund, P. Karlsson, B. Wannberg, R. W. Carpick, Rev. Sci. Instrum., in press (2012).
12. J. Tersoff, Phys. Rev. Lett. **61** (1988) 2879.
13. J. Tersoff, Phys. Rev. B **37** (1988) 6991.
14. J. Tersoff, Phys. Rev. B **39** (1989) 5566.

15. M. F. Yu, O. Lourie, M. J. Dyer, K. Moloni, T. F. Kelly, R. S. Ruoff, *Science* **287** (2000) 637.
16. Y. J. Jeong, S. I. Cha, K. T. Kim, K. H. Lee, C.B. Mo, S. H. Hong, *Small* **3** (2007) 840.
17. H. Li, A. Misra, Z. Horita, C. C. Koch, N. A. Mara, P. O. Dickerson, *Appl. Phys. Lett.* **95** (2009) 71907.
18. R.V. Noorden, *Nature* **469** (2011) 14.
19. J. Schiøtz, K. W. Jacobsen, *Science* **301** (2003) 1357.
20. M. R. Falvo, G. J. Clary, R. M. Taylor, .V Chi, F. P. Brooks, S. Washburn, *Nature* **389** (1997) 582.
21. K. Mylvaganam, L. C. Zhang, *Nanotechnology* **17** (2006) 410.
22. P. D. Bradford, X. Wang, H. Zhao, Y. T. Zhu, *Carbon* **49** (2011) 2834.
23. A. Pantano, D. M. Parks, M. C. Boyce, *J. Mech. Phys. Solids* **52** (2004) 789.
24. B. I. Yakobson, C. J. Brabec, J. Bernholc, *Phys. Rev. Lett.* **76** (1996) 2511.
25. Y. R. Jeng, .P C. Tsai, T. H. Fang, *Appl. Phys. Lett.* **90** (2007) 161913.
26. E. T. Thostenson, T. W. Chou, *Carbon* **42** (2004) 3015.
27. J. F. Waters, L. Riestler, M. Jouzi, P. R. Guduru, J. M. Xu, *Appl. Phys. Lett.* **85** (2004) 1787.
28. J. F. Waters, P. R. Guduru, M. Jouzi, J. M. Xu, T. Hanlon, S. Suresh, *Appl. Phys. Lett.* **87** (2005) 103109.
29. W. G. Hoover, *Phys. Rev. A* **31** (1985) 1695.
30. C. Y. Tang, L. C. Zhang, *Nanotechnology* **16** (2005) 15.
31. B. Luan, M. O. Robbins, *Nature* **435** (2005) 929.
32. Y. R. Jeng, S. R. Peng, *Appl. Phys. Lett.* **94** (2009) 163103.
33. B. Li, P. C. Clapp, J. A. Rifkin, X.M. Zhang, *J. Appl. Phys.* **90** (2001) 3090.
34. D. Mulliah, S. D. Kenny, R. Smith, *Phys. Rev. B* **69** (2004) 205407.

35. R. W. Carpick, D. F. Ogletree, M. Salmeron, *Appl. Phys. Lett.* **70** (1997) 1548.
36. A. Socoliuc, R. Bennewitz, E. Gnecco, E. Meyer, *Phys. Rev. B* **92** (2004) 134301.
37. V. Brizmer, Y. Kligerman, I. Etsion, *ASME J. Tribol.* **129** (2007) 783.
38. Y. C. Wu, G. G. Adams, *ASME J. Tribol.* **131** (2009) 011403.
39. K. L. Johnson, *Contact Mechanics*, Cambridge University Press, UK, 1985.
40. D. Tabor, *Proc. R. Soc. Lond. Ser. A* **251** (1959) 378.
41. F. P. Bowden, J. E. Young, *Proc. R. Soc. Lond. Ser. A* **208** (1951) 311.
42. Y. R. Jeng, C. M. Tan, *Appl. Phys. Lett.* **89** (2006) 251901.

List of Publications

C. R. Das, S. Dhrar, Yeau-Ren Jeng, P. C. Tsai, H. C. Hsu, Baldev Raj, A. K. Bhaduri, S. K. Albert, A. K. Tyagi, L. C. Chen, and K. H. Chen, 2010, "Direct Observation of Amorphization in Load Rate Dependent Nanoindentation Studies of Crystalline Si," Applied Physics Letters, Vol. 96, Issue 25, 253113 (SCI)

Yeau-Ren Jeng, Chien-Ping Mao, 2010, "The effect of contaminants on the adhesion of the spatulae of a gecko," Journal of Biosciences, Vol. 35, Issue 4, pp. 595-603 (SCI)

Meng-Hung Lin, Yeau-Ren Jeng, Chang-Pin Chou, Hua-Chiang Wen, 2010, "Nanoscratch Characterization of GaN Epilayers on c- and a-Axis Sapphire Substrates," Journal of Nanoscale Research Letters, Vol. 5, Issue 11, pp. 1812-1816 (SCI)

Meng-Hung Lin, Yeau-Ren Jeng, Chang-Pin Chou, Hua-Chiang Wen, 2010, "Nanoscratch Characterization of GaN Epilayers on c- and a-Axis Sapphire Substrates," Journal of Nanoscale Research Letters, Vol. 5, Issue 11, pp. 1812-1816 (SCI)

Song-Jeng Huang, Yeau-Ren Jeng, V. I. Semenov, Yo-Zhi Dai, 2011, "Particle Size Effects of Silicon Carbide on Wear Behavior of SiCp-Reinforced Magnesium Matrix Composites," Tribology Letters, Vol. 42, No. 1, pp. 79-87 (SCI)

Yeau-Ren Jeng, Tsung-Ting Lin, Hsiu-Ming Hsu, Hsin-Ju Chang, Dar-Bin Shieh, 2011, "Human Enamel Rod Presents Anisotropic Nanotribological Properties," Journal of the Mechanical Behavior of Biomedical Materials, Vol. 4, Issue 4, pp. 515-522 (SCI)

Kuo-Cheng Chen, Franklin Chau-Nan Hong, Yeau-Ren Jeng, 2011, "Deposition of Titania-containing Diamond-like Carbon Nanocomposite Films by Sputtering-assisted Chemical Vapor Deposition," Journal of the Plasma Processes and Polymers, Vol. 8, Issue 4, pp. 324-332 (SCI)

Hung-Chang Li, K. Koteswara Rao, Jun-Yuan Jeng, Yu-Jer Hsiao, Tzung-Fang Guo, Yeau-Ren Jeng, Ten-Chin Wen, 2011, "Nano-scale Mechanical Properties of Polymer/Fullerene Bulk Hetero-junction Films and Their Influence on Photovoltaic Cells," Solar Energy Materials & Solar Cells, Vol. 95, Issue 11, pp. 2976-2980 (SCI)

Yu-Lin Hsin, Hsiao-Yeh Chu, Yeau-Ren Jeng, Yao-Huei Huang, Mei-Hua

Wang, Chih-Kuang Chang, 2011, "In-situ De-agglomeration and Surface Functionalization of Detonation Nanodiamond With the Polymer Used as an Additive in Lubricant Oil," *Journal of Materials Chemistry*, Vol. 21, pp. 13213-13222 (SCI)

Chih-Jung Chen, Ray-Kuang Chiang, Yeau-Ren Jeng, 2011, "Crystallization and Magnetic Properties of 3D Micrometer-Scale Simple-Cubic Magnetite Superlattices," *Journal of Physical Chemistry C*, Vol. 115, pp. 18142-18148 (SCI)

Yeau-Ren Jeng, Shin-Rung Peng, 2012, "Atomic Simulation of Contact Behavior during Sliding Inception of an Asperity," *Wear*, Vol. 276-277, pp. 70-74 (SCI)

Shyh-Chi Wu, Yeau-Ren Jeng, Wei-Hung Yau, Kuan-Te Wu, Chien-Huang Tsai, Chang-Pin Chou, 2012, "Nanoindentation response of zinc titanate thin films deposited by co-sputtering process," *Applied Surface Science*, Vol. 258, Issue 18, pp. 6730-6734

Yeau-Ren Jeng, C.-M. Tan, C. C. Su, S.-C. Cheng, C.-Y. Cheng, 2012, "Experimental Study on the Nanoindentation of Thin Copper Films from Deep Submicron to Nano-Scale," *Journal of Mechanics*, Vol. 28, Issue 3, pp. 507-511 (SCI)

Yeau-Ren Jeng, Yi-Min Wang, Hua-Chiang Wen, Shih-Ming Huang, Franklin Chau-Nan Hong, Ching-Yang Cheng, 2012, "Effect of Feed Gas Composition Effects on Nanotribological Properties of Diamond-like Carbon Films," *Thin Solid Films*, (SCI) (in press).

F. Mangolini, J. Åhlund, G.E. Wabiszewski, V.P. Adiga, P. Egberts, F. Streller, K. Backlund, P. Karlsson, B. Wannberg, and R.W. Carpick, 2012, "Angle-Resolved Environmental X-Ray Photoelectron Spectroscopy: a New Laboratory Setup for Photoemission Studies at Pressures up to 0.4 Torr," *Rev. Sci. Instrum.*, (SCI) (in press).

Yeau-Ren Jeng and Ping-Chi Tsai, 2012, "Buckling-assisted Strengthening of Carbon Nanotube Reinforced Copper Matrix Nanocomposites," *Composites Science and Technology* (revised) (SCI)

Yeau-Ren Jeng, Ping-Chi Tsai, Shang-Hsuan Chiang and Chuan-Pu Liu, 2012, "Effects of Grain Size and Preferred Orientation of Nanocrystalline Nickel Films on Mechanical and Tribological Properties," *Wear* (revised) (SCI)

Yeau-Ren Jeng, Ping-Chi Tsai, Chien-Ping Mao, Kuan-Te Wu and Franklin Chau-Nan Hong, 2012, "Effects of Surface Morphology, Size Effect and Wettability on Interfacial Adhesion of Carbon Nanotube Arrays," Thin Solid Film (revised) (SCI)

Keynote Speaker of International Conference, Invited Seminar International Conference

Yeau-Ren Jeng, 2010, "Nanomechanics of Asperity Contact: Multi-scale Perceptiive of Two Configurations," Invited Lecture, The 12th International Congress on Mesomechanics, Taipei, Taiwan, June 21-26

Yeau-Ren Jeng, 2010, "Atomistic Investigation of Tribological Contacts," Invited Keynote Speaker for Tribology Symposium of the Fifth International Conference Multiscale Materials Modeling, Freiburg, Germany, Oct. 4-8

Yeau-Ren Jeng, 2010, "Computations as Tools of Development and Discovery," National Center for High-Performance Computing, Keynote Speaker, Hsinchu, Taiwan, Nov.4

Yeau-Ren Jeng, 2012, "Challenge & Future Direction of Advanced Manufacturing," 1st International Advisory Board Meeting, Advanced Institute of Manufacturing with High-tech Innovations, Keynote Speaker, Chiayi, Taiwan, February 14-15.

Yeau-Ren Jeng, 2012, "Challenge & Future Direction of Advanced Manufacturing System: AIM-HI Perspective," The 4th International Conference on Advanced Manufacturing, Society of Manufacturing Engineers, Keynote Speaker, Yilan, Taiwan, March 4-8.

Invited Speaker of International Conference

Yeau-Ren Jeng, 2010, "Multi-scale Investigation of Asperity Contact: A Study of Nanomechanics," Invited Speaker, The 7th Taiwan/U.S. Air Force Nanoscience Workshop, National Science and Technology Program for Nanoscience and Nanotechnology, Yilan, Taiwan, March 31-April 3

Yeau-Ren Jeng, 2010, "Multi-scale Perspective of Asperity Contact:

Nanomechanics Investigation of Two Configurations,” Invited Speaker, International Workshop on Materials Behavior at the Micro- and Nano- Scale, Xi' an, China, June 8-11

Yeau-Ren Jeng, 2010, “Lesson learned from Characterization of Nano-scale Mechanical Properties,” Invited Speaker, The 8th Cross-Strait Workshop on Nano Science and Technology, Hong Kong, China, Dec. 20-22

Yeau-Ren Jeng, 2011, “Atomistic Investigation of Asperity Contact: A Study of Two Configurations,” 8th Taiwan/U.S. Air Force Nanoscience Workshop, Invited Speaker, Seattle, WA, U.S.A., April 5-6

R.W. Carpick, “Geometrical effects in contact mechanics: From atomic membranes to evolving asperities,” Invited Speaker, Eighth International Conference on Flow Dynamics, Sendai, Japan, Nov. 2011.

R.W. Carpick, “Atomic-Scale Friction and Wear of Single Asperities,” Invited Speaker, Joint ICTP-FANAS Conference on Trends in Nanotribology, Abdus Salam International Centre for Theoretical Physics (ICTP), Trieste, Italy, Sept. 2011.

Yeau-Ren Jeng, 2012, “Toward in-situ observation of micro-structure changes of nanomaterials,” 9th Taiwan/U.S. Air Force Nanoscience Workshop, Invited Speaker, Kenting, Taiwan, April 17-20

R.W. Carpick, “Evolving Asperities to 2-D Atomic Membranes,” Invited Speaker, Upcoming: ASME International Mechanical Engineering Congress & Exposition (IMECE), Houston, TX, Nov. 2012.

R.W. Carpick, “Nanoscale Wear as a Stress-Assisted Chemical Reaction,” Invited Speaker, 4th International Workshop on Materials Behavior at the Micro- and Nano- Scale, Xi'An, China, Jun. 2012.

R.W. Carpick, “ Kinetic Processes in Nanotribology,” Invited Speaker, Workshop on Fundamental Aspects of Friction and Lubrication, Lorentz Center, Leiden, Netherlands, Apr. 2012.